Journal of Computational Physics 229 (2010) 2605–2624

Contents lists available at ScienceDirect

Journal of Computational Physics

journal homepage: www.elsevier.com/locate/jcp

A Legendre spectral element model for sloshing and acoustic analysis in nearly incompressible fluids

D. Krishna Kishor, S. Gopalakrishnan *, Ranjan Ganguli

Department of Aerospace Engineering, Indian Institute of Science, Bangalore, India

ARTICLE INFO

Article history:
Received 21 July 2009
Received in revised form 5 December 2009
Accepted 7 December 2009
Available online 16 December 2009

Keywords:
Legendre polynomials
Acoustic fluids
Sloshing motion
Incompressible locking
Numerical integration
Linear elements

ABSTRACT

A new spectral finite element formulation is presented for modeling the sloshing and the acoustic waves in nearly incompressible fluids. The formulation makes use of the Legendre polynomials in deriving the finite element interpolation shape functions in the Lagrangian frame of reference. The formulated element uses *Gauss–Lobatto–Legendre* quadrature scheme for integrating the volumetric stiffness and the mass matrices while the conventional *Gauss–Legendre* quadrature scheme is used on the rotational stiffness matrix to completely eliminate the zero energy modes, which are normally associated with the Lagrangian FE formulation. The numerical performance of the spectral element formulated here is examined by doing the inf–sup test on a standard rectangular rigid tank partially filled with liquid. The eigenvalues obtained from the formulated spectral element are compared with the conventional equally spaced node locations of the *h*-type Lagrangian finite element and the predicted results show that these spectral elements are more accurate and give superior convergence. The efficiency and robustness of the formulated elements are demonstrated by solving few standard problems involving free vibration and dynamic response analysis with undistorted and distorted spectral elements, and the obtained results are compared with available results in the published literature.

1. Introduction

Fluid elements formulated using Lagrangian frame of reference have displacements as nodal degrees of freedom. The main advantage of such a formulation is in modeling the fluid–structure interaction problems, where in explicit coupling of the fluid and the structure degrees of freedom at the fluid–solid interface is not required. Assembly of finite element matrices and enforcement of multipoint constraints between the fluid and the solid degrees of freedom along the fluid–solid interface would ensure coupling of the two domains. However, such a procedure would give rise to other problems such as (i) mesh locking due to fluid incompressibility. (ii) The second problem associated with the Lagrangian finite element formulation is the presence of zero energy modes due to fluid circulation. These zero energy modes enormously increase the computational cost of the eigenvalue analysis.

Mesh locking in the *h*-type finite elements is a well researched area. In solids, mesh locking occurs due to shear in rod and beam elements, membrane locking in curved elements and volumetric locking in nearly incompressible medium. There are many ways to alleviate the mesh locking in finite elements. The most common method is to make the matrices associated with the constraint field rank deficient by reduced integration. Refs. [1–6] report these methods for different naturally occurring constraints in the *h*-type finite elements in solid mechanics. The second method of alleviating mesh locking is through

* Corresponding author. Fax: +91 080 3600134.
E-mail address: krishnan@aero.iisc.ernet.in (S. Gopalakrishnan).

0021-9991/$ - see front matter © 2009 Elsevier Inc. All rights reserved.
doi:10.1016/j.jcp.2009.12.008

field consistent approach [7–9]. Here, the constraint strain fields are smoothed using appropriate Legendre polynomials. This approach is reported in Refs. [7–9] to handle mesh locking in the *h*-type solid beam, plate and shell elements to remove locking due to shear, membrane effects and incompressibility. Papers by authors [10,11] have shown the ability of the field consistent approach to remove mesh locking due to fluid incompressibility in Lagrangian *h*-type 2-D and 3-D fluid finite elements. The reported *h*-type finite elements [1–11] showed algebraic convergence with reduced order Gauss quadrature on the constrained stiffness matrices, and with full Gauss quadrature on the consistently formulated stiffness matrices.

As mentioned earlier, modeling fluids in displacement-based Lagrangian frame of reference results in large number of zero energy modes which are attributed to the fluid circulation. These modes are of little interest to an analyst and they contribute to the enormous drain in the computational resources. Refs. [10–15] suggested that these zero energy modes can be pushed further in the eigenspace by converting them into high frequency rotational modes by making the fluid irrotational. That is, an additional vorticity vector is introduced in the constitutive model by relating the stress due to fluid irrotationality with the fluid vorticity by a constant called rotational modulus (R). Although, this procedure eliminates all the zero energy modes, the vorticity introduced in the constitutive model increases the stiffness of the fluid element further with increase in R and the low frequency slosh modes are not captured accurately. Since, the rotational constraint is a weak constraint, the finite element matrices associated with this constraint need to be integrated with an appropriate integration order that can convert these unwanted zero energy modes to rotational modes. Refs. [10,11] show how such a procedure would give superior results for the fluid domain modeled using the *h*-type 2-D and 3-D Lagrangian fluid finite elements. Moreover, the *h*-type finite element solution converges at the rate of $\frac{1}{N^{p+1}}$, where N is the total number of degrees of freedom in the model and p is the polynomial order of the interpolation function used in the element formulation. Hence, for a given polynomial order p, the fine mesh results in greater value of N, which results in higher convergence rate for a fixed value of p.

The *p*-version of the finite element formulation is frequently used as an efficient alternative to the *h*-type finite elements, since locking effects are avoided *a priori* [16]. However, in the case of nearly incompressible material behaviour, higher order Lagrangian fluid elements ($p = 2, 3$) suffer from volumetric locking phenomena [10,11]. In the *p*-type finite elements, the spatial domain is discretized with the *h*-type Lagrangian elements, and the solution accuracy is improved by increasing the polynomial order p of the element shape functions, thereby increasing the number of degrees of freedom in an invariant mesh of the same elements. For sufficiently smooth problems, *p*-type elements exhibit highly desirable *exponential* convergence, *i.e.*, error is proportional to $e^{-\beta N}$ for some constant β [17].

The *p*-type finite elements uses *hierarchical* polynomial shape functions [17,28]. For an element of order p, these shape functions constitute a subset of those for an element of order $(p + 1)$. While such shape functions do not constitute a nodal basis as Lagrangian interpolants do, they are well suited to adaptive refinement, which is very common in fluid dynamics [18]. However, hierarchical finite elements do have full mass matrices, which have no satisfactory diagonalization scheme [19] and in addition diagonal mass matrices are preferred for explicit time integration.

Spectral elements are a new class of finite elements having superior convergence properties. These elements are constructed by using Lagrangian interpolation functions which uses either the Legendre, the Chebyshev or the Laguerre polynomials. Spectral finite elements [20] are also *p*-type finite elements, but their shape functions are formed using the Lagrangian interpolants with their node point locations at either the $(p + 1)$ *Gauss–Lobatto–Chebyshev* (*GLC*) or *Gauss–Lobatto–Legendre* (*GLL*) points. Spectral finite elements combine the accuracy of the global spectral methods [21,22] with the geometric flexibility of the *h*-type finite elements. Spectral finite elements have been extensively and successfully used in fluid dynamics [20,23], acoustics [24], and geophysics [25]. However, to the best of author's knowledge, there has been not any spectral finite element formulation to model the acoustic fluids in nearly incompressible limit to calculate the slosh and the acoustic wave motions. This paper constitutes an exploratory study of this application.

One of the main difference between the *h*-type and the spectral finite elements is that in the case of Legendre spectral finite elements, the node point locations and the quadrature point locations will be same but, not in the *h*-type elements. This coincidence of the node point and the quadrature point locations provides a diagonal mass matrix [25] and this nodal lumping quadrature [26,27] has also been termed as optimal lumping [6]. Here, we use *Gauss–Lobatto–Legendre* (*GLL*) node locations since these Legendre polynomials are orthogonal with respect to the unity weighting function, whereas Chebyshev polynomials are not orthogonal to the unity weighting function [31]. Moreover, the Chebyshev points are appropriate for integration with respect to the $1/(1-\xi^2)^{1/2}$ weighting function, not the unity weighting function, and the required order of quadrature accuracy would not be achieved [32].

This coincident node point and (*GLL*) quadrature points seem restrictive in some special problems. The authors tried in the present paper to explore this restrictive nature of the coincident node and the quadrature points. As one could use the non-nodal quadrature schemes (*i.e., Gauss–Legendre*), still using the same Legendre spectral element shape functions derived using the $(p + 1)$ *GLL* points. The authors have tried in the present paper both techniques of using the nodal quadrature and the non-nodal quadrature schemes for evaluating the finite element matrices. First, $(p + 1) \times (p + 1)$ *GLL* quadrature on both the stiffness (volumetric and rotational) and the mass matrices for an element with shape function polynomial order of (p) is employed. Later, the authors have tried mixed quadrature technique, where, the non-nodal quadrature scheme (*Gauss–Legendre* (*GL*)) on the rotational stiffness matrix and the *GLL* quadrature on the volumetric stiffness and the mass matrices is employed. These aspects will be looked into great detail in this paper.

As said earlier, mesh locking occurs in the finite elements due to various constraints. One way to measure the locking in the finite elements is through the patch test or the inf–sup test. If a material is subjected to two constraints, *i.e.*, incompressibility and irrotationality like in the present case, the inf–sup test is a favorable tool to apply. Authors in [10,11] used this inf–

sup test to find whether the formulated consistent Lagrangian fluid finite elements [10,11] locks in the incompressible limit as the mesh is refined. The inf–sup test can be a difficult criterion to apply to a new formulation [35–38]. Here, we use this inf–sup test to study the performance of the newly formulated Legendre spectral finite element under twin constraints namely incompressibility and irrotationality.

The remainder of this paper is outlined as follows: in Section 2, we derive the formulation of low order *h*-type Lagrangian finite elements and the Legendre spectral finite elements for the acoustic wave equation to calculate the sloshing and the volume change frequencies. In Section 3, we compare the results of the *h*-type and the Legendre spectral finite elements in predicting the slosh and the acoustic frequencies followed by the inf–sup test, where the performance of the formulated elements is evaluated, and the convergence studies and the dynamic analysis is carried out in the succeeding sections. The paper ends with the conclusions in Section 4.

2. Finite element formulation

In this section, we introduce the formulation of both the *h*-type and the Legendre polynomials based spectral FE formulation. Since, the *h*-type FE formulation is quite well known and its application to the fluid problems is reported in [10,11], we provide only a brief introduction to its formulation here for the sake of completeness. In deriving the governing differential equations for the fluid, we make the usual acoustic wave theory approximations [12]. That is the fluid motion is assumed to be inviscid, compressible, and adiabatic. Body forces are neglected. Also, the fluid density is taken to be a function of pressure only (not temperature) so that the density is barotropic.

An important behavior of the fluid system is the ability to displace without a change in the volume. For bounded free surface fluid systems, the free surface of the fluid will move vertically by the so called sloshing waves. These sloshing waves, in a steady-state condition, involve a harmonic interchange of the kinetic and the potential energy of the fluid system. The relatively low frequency sloshing behaviour of a fluid system involves incompressible modes of displacements which result in relatively large vertical surface displacements. The total potential energy of the fluid system (Π_P), consists of sum of the strain energy Π_E, due to compressibility and irrotationality, and the energy due to free surface oscillations of the fluid Π_S, which can be written as

$$\Pi_P = \Pi_E + \Pi_S. \tag{1}$$

Here

$$\Pi_E = \frac{1}{2}\int_\Omega \{\varepsilon\}^T[\mathbf{C}]\{\varepsilon\}d\Omega \tag{2}$$

and

$$\Pi_S = \frac{1}{2}\int_S \rho g\{u_s\}^T\{u_s\}dS, \tag{3}$$

where $\{\varepsilon\}$ is a strain vector of volumetric, rotational and shear strains which is given as, $\{\varepsilon\} = [\varepsilon_v, \varepsilon_z, \gamma_{xy}]^T$. Small amount of shear (γ_{xy}) is added to the potential energy of the fluid for stability of the solution [6], and [**C**] is a diagonal material matrix given by

$$[\mathbf{C}] = \begin{bmatrix} K & 0 & 0 \\ 0 & R & 0 \\ 0 & 0 & G \end{bmatrix}, \tag{4}$$

where K is the bulk modulus, R is the rotational modulus and G is the shear modulus of the fluid. The value of R is usually chosen as $100K$ as suggested by Wilson and Khalvathi [13] and $\{u_s\}$ is the free surface displacement vector of the fluid on the surface S, ρ is the mass density of the fluid, g is the acceleration due to gravity and Ω is the volume of the entire fluid domain. The kinetic energy (Π_T) of the fluid is given by

$$\Pi_T = \frac{1}{2}\int_\Omega \rho\{V\}^T\{V\}d\Omega, \quad \{V\}^T = \{\dot{u}, \dot{v}\}, \tag{5}$$

where $\{V\}$ is the velocity vector in cartesian co-ordinates.

2.1. Finite element matrices

The displacement fields u and v in the *h*-type and the *Legendre spectral* finite element can be written as

$$u(x,y) = \sum_{i=1}^{q} N_i(\xi,\eta)u_i, \quad v(x,y) = \sum_{i=1}^{q} N_i(\xi,\eta)v_i, \tag{6}$$

where q is the number of nodes on each element. Here ξ and η are the mapped isoparametric co-ordinates and N_i's are the shape functions of these elements in the mapped co-ordinates. The strain displacement relation can be written as

$$\{\varepsilon\} = [\mathbf{B}]\{d_1\}, \quad \{\varepsilon\} = \{\varepsilon_v, \varepsilon_z, \gamma_{xy}\}^T. \tag{7}$$

Here [**B**] is the strain displacement matrix. The volumetric, rotational and the shear strains are given by

$$\varepsilon_v = \left(\frac{\partial u}{\partial x} + \frac{\partial v}{\partial y}\right), \tag{8}$$

$$\varepsilon_z = \frac{1}{2}\left[\frac{\partial v}{\partial x} - \frac{\partial u}{\partial y}\right], \tag{9}$$

$$\gamma_{xy} = \left(\frac{\partial u}{\partial y} + \frac{\partial v}{\partial x}\right) \tag{10}$$

re-writing Eq. (7) as

$$\{\varepsilon\} = \begin{bmatrix} [B_V] \\ [B_R] \\ [B_G] \end{bmatrix} \{d_1\} = [\mathbf{B}]\{d_1\}, \tag{11}$$

where $[B_V]$ is the strain displacement matrix for the volumetric strain, $[B_R]$ is the strain displacement matrix for the rotational strain and $[B_G]$ is the strain displacement matrix for the shear strain, and $\{d_1\}$ is given as $\{d_1\}^T = \{u_1, v_1, u_2, v_2, \ldots, u_q, v_q\}$, where q is the number of nodes in the element.

The discrete form of the governing equations can be obtained by applying the Hamilton's principle, which can be written as

$$\delta \int_{t_1}^{t_2} (\Pi_T - \Pi_P + W_{nc}) dt = 0, \tag{12}$$

where W_{nc} is the non-conservative energy due to applied forces and damping. The discrete equations can be written as

$$[\mathbf{M}]\{\ddot{u}\} + [\mathbf{K}]\{u\} + [\mathbf{K}_s]\{u_s\} = \{F\}, \tag{13}$$

where $\{\ddot{u}\}$ is the vector of nodal accelerations, $\{u_s\}$ is the displacement vector of free surface elements, $\{F\}$ is the applied force vector and $[\mathbf{K}_s]$ is the slosh stiffness matrix. The mass matrix [**M**] and the stiffness matrix [**K**] are symmetric and banded, and they are given by

$$[\mathbf{M}] = \int_\Omega \rho [N]^T [N] d\Omega, \quad [\mathbf{K}] = \int_\Omega [B]^T [\mathbf{C}][B] d\Omega. \tag{14}$$

The diagonal constitutive matrix [**C**] enables easy splitting of the stiffness matrix [**K**] into the volumetric stiffness $[\mathbf{K}_V]$, the rotational stiffness $[\mathbf{K}_R]$ and the shear stiffness $[\mathbf{K}_G]$ and this is given below,

$$[\mathbf{K}] = \int_\Omega [B_V]^T K [B_V] d\Omega + \int_\Omega [B_R]^T R [B_R] d\Omega + \int_\Omega [B_G]^T G [B_G] d\Omega,$$

which can be written as

$$[\mathbf{K}] = [\mathbf{K}_V] + [\mathbf{K}_R] + [\mathbf{K}_G]. \tag{15}$$

The sloshing stiffness matrix is given by

$$[\mathbf{K}_s] = \int_S \rho g [N_s]^T [N_s] dS \tag{16}$$

The surface of the fluid is modeled as a one-dimensional line element. The shape functions $[N_s]$ are obtained using the Lagrangian interpolation formula. The slosh stiffness matrix in Eq. (16) is evaluated and added only to the vertical degrees of freedom of the stiffness matrix in Eq. (15) that correspond to the free surface nodes.

2.2. h-Type finite elements

Here, we derive the *h*-type finite elements which will be used to evaluate the integrals in Eqs. (14) and (16). The displacement-based Lagrangian interpolation polynomial $L_j(\xi^k)$, related to node j and expressed in terms of natural co-ordinates ξ^k, where $k = 1, 2$ for two dimensions and $k = 1, 2, 3$ for three dimensions are defined by

$$L_j(\xi^k) = \prod_{\substack{i=1 \\ i \neq j}}^{p+1} \frac{(\xi^k - \xi_i)}{\xi_j - \xi_i}. \tag{17}$$

An attractive feature of the Lagrangian interpolants is that they constitute a nodal basis, *i.e.*,

$$L_j(\xi_i) = \delta_{ij},$$

where δ_{ij} is the Kronecker delta function. Here, the $(p+1)$ nodes are chosen evenly within the element itself. The $L_j(\xi^k)$ is the pth-order Lagrangian interpolation polynomial associated with node j. The solution accuracy is increased by increasing the number of elements in the finite element model while keeping the same interpolation polynomial order (p). In the present analysis, we have used linear h-type elements [10]. In evaluating the finite element stiffness matrix, different order *Gauss-quadrature* is employed and obtained results are compared with newly formulated Legendre spectral element results in Section 3.

2.3. Legendre spectral finite elements

In the Legendre spectral finite elements, we use the same Lagrangian interpolation function as used in Eq. (17) for the h-type finite elements. However, the main difference between these two methods is in the location of the nodes in the finite element. Here, the $(p+1)$-point node locations are at the zeros of the following polynomial equation:

$$f_p(\xi^k) = (1 - (\xi^k)^2) \cdot P'_p(\xi^k). \tag{18}$$

The zeros of the above equation are identical to the positions of the *Gauss–Lobatto–Legendre* (*GLL*) points, where $P_p(\xi^k)$ describes the pth order Legendre polynomial with the interval $[-1\ 1]$, which is given by

$$\begin{aligned} &P_0^k = 1, \quad P_1^k = \xi^k, \quad P_2^k = \frac{1}{2}[3 \cdot (\xi^k)^2 - 1], \quad P_3^k = \frac{[5 \cdot (\xi^k)^3 - 3 \cdot \xi^k]}{2}, \\ &P_p^k = \frac{[2 \cdot p - 1]}{p} \cdot \xi^k \cdot P_{p-1}^k - \frac{[p-1]}{p} \cdot P_{p-2}^k, \quad p \geqslant 2, \end{aligned} \tag{19}$$

where p denotes the polynomial order. These *Gauss–Lobatto–Legendre* points reduce oscillations of the corresponding shape functions [29]. They are characterized by the property,

$$\int_{-1}^{+1} \int_{-1}^{+1} P_i^1 \cdot P_j^2 \cdot P_k^1 \cdot P_l^2 \, d\xi^1 \, d\xi^2 = \begin{cases} \neq 0 & \text{for } i = k, j = l, \\ = 0 & \text{else}, \end{cases} \tag{20}$$

where $i, j, k, l = 0, 1, 2, \ldots, p$ [30]. The 2-D shape functions are obtained by the product of two 1-D shape functions,

$$N_n = N_{ij}(\xi^1, \xi^2) = L_i(\xi^1) \cdot L_j(\xi^2)$$

with $i = 1, 2, 3, \ldots, p+1$ and $j = 1, 2, 3, \ldots, p+1$ for all nodes 'n' of each element, where $n = 1, 2, 3, \ldots, (p+1)^2$. The approximation of the kinematic quantities using the above shape functions are given by

$$x^k = \sum_{n=1}^{(p+1)^2} N_n \cdot x_n^k, \quad u^k = \sum_{n=1}^{(p+1)^2} N_n \cdot u_n^k,$$

where $k = 1, 2$ for 2-D cases and $k = 1, 2, 3$ for 3-D cases.

An important difference between the h-type finite elements and the Legendre spectral finite elements as discussed in the introduction is the location of the node points and the quadrature rule. In the Legendre spectral finite elements, the node points are located at the $(p+1)$ *Gauss–Lobatto–Legendre* points and the same $(p+1)$-point *GLL* quadrature is employed. Such quadrature is only exact for polynomials of degree $\leqslant (2p-1)$ in 1-D elements [31]. As such, the *GLL* quadrature scheme is exact for the stiffness matrices, but constitutes a reduced quadrature scheme for the mass-type matrices [31]. In the case of 2-D finite elements, $(p+1) \times (p+1)$ *GLL* quadrature constitutes a reduced quadrature scheme (underintegration) [33]. The coincident node and quadrature points produce optimally lumped mass-type matrices [6]. In the present paper, we have considered polynomials up to an order of $p = 7$ for the spectral finite element formulation. In the h-type finite elements, the node point locations and the quadrature point locations are different. The node point locations are evenly distributed within the finite element and the quadrature points are at the zeros of the Legendre polynomials.

3. Numerical experiments

In this section, we calculate the slosh and the acoustic frequencies of the bounded liquid in a rigid rectangular tank using the spectral element formulation developed in the previous section. The exact slosh frequencies along with their mode shapes are given by [39]

$$\omega_{mn}^2 = gk \tanh(kh), \tag{21}$$

where

$$k^2 = \pi^2 \left(\frac{m^2}{b^2} + \frac{n^2}{a^2} \right)$$

and the mode shapes are given by

$$\delta = \sum_{m=0}^{\infty}\sum_{n=0}^{\infty} A_{mn}\cos\left[\left(\frac{m\pi}{b}\left(x+\frac{b}{2}\right)\right)\right]\times\cos\left[\left(\frac{n\pi}{a}\left(z+\frac{a}{2}\right)\right)\right], \tag{22}$$

m, n are integers ranging from 0 to ∞, and δ is the elevation of the liquid and b, a and h are rectangular tank length, breadth and height, respectively. The acoustic frequencies are given by [12]

$$\omega = c\lambda = c\pi\left[\left(\frac{n}{b}\right)^2+\left(\frac{m}{2h}\right)^2\right]^{1/2} \tag{23}$$

and the mode shapes are,

$$\delta_1 = A\lambda_1\sin(\lambda ct)\cos(\lambda_2 y)\sin(\lambda_1 x),$$
$$\delta_2 = A\lambda_2\sin(\lambda ct)\sin(\lambda_2 y)\cos(\lambda_1 x),$$

where

$$\lambda_1 = n\pi/b, \quad n = 0,1,2,3\ldots,$$
$$\lambda_2 = m\pi/2h, \quad m = 1,3,5\ldots$$

and

$$\lambda = \sqrt{\lambda_1^2+\lambda_2^2} \quad \text{and} \quad \delta = \sqrt{\delta_1^2+\delta_2^2}, \tag{24}$$

c is the speed of the acoustic waves and δ is the free surface elevation of the liquid.

The dimensions of the tank are as follows: The length b is 5.08 m and height h is 1.905 m, and the finite element discretization of the domain is shown in Fig. 1(a).

The following material properties for the fluid are chosen: $K = 2.07\times10^9$ N/m^2, $R = 100K$, and $\rho = 1000$ kg/m^3. The acceleration due to gravity g is taken as 9.8 m/s^2. Here, we study the behaviour of each Legendre spectral element formulated in Section 2.3 with different shape function polynomial order (p). Using this formulated Legendre element, the fluid domain shown in Fig. 1(a) is modeled and solved the eigenvalue problem associated with Eq. (13). From the eigenvalue analysis, the number of zero energy modes, slosh modes, rotational modes, acoustic and the mixed modes are calculated. Rotational constraint is imposed on the Legendre spectral element to reduce or completely eliminate the number of zero energy modes which are inherent in the fluid elements formulated based on the Lagrangian frame of reference. The effect of rotational constraint on generation of number of specific modes is studied in the following sections, to understand as to what integration scheme should be applied on the rotational stiffness matrix.

3.1. Effect of numerical integration rule on natural frequencies

In the finite element analysis, the problem domain shown in Fig. 1(a) is discretized with one Legendre spectral finite element. We solve the eigenvalue problem associated with Eq. (13) to get the first few slosh and acoustic frequencies. The exact frequencies of first few slosh and acoustic modes are taken from [10]. They are given here to compare with the FE results obtained in the following sections. The slosh frequencies are: $\omega_{sl1} = 2.2385$ rad/s, $\omega_{sl2} = 3.4504$ rad/s, $\omega_{sl3} =$

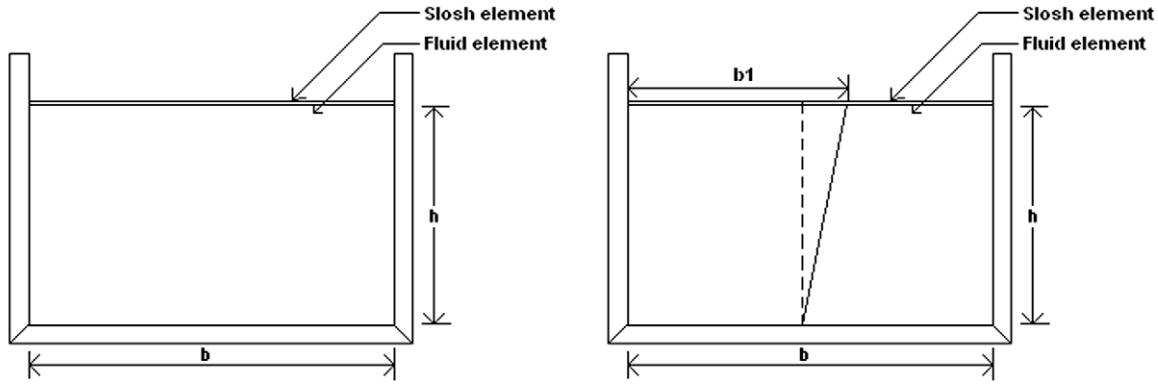

(a) 2-D finite element discretization of a rectangular tank

(b) 2-D finite element discretization of a rectangular tank with two distorted spectral elements

Fig. 1. 2-D finite element discretization of rectangular tank with undistorted and distorted spectral elements.

4.2603 rad/s, $\omega_{sl4} = 4.9232$ rad/s, $\omega_{sl5} = 5.5047$ rad/s, and $\omega_{sl6} = 6.0310$ rad/s, and the acoustic frequencies are $\omega_{ac1} = 1185.8$ rad/s, $\omega_{ac2} = 1482.2$ rad/s, $\omega_{ac3} = 2137.7$ rad/s, $\omega_{ac4} = 3557.1$ rad/s and $\omega_{ac5} = 3666.7$ rad/s.

In the *GLL*-quadrature, we do not have 1-point quadrature scheme, where the integration order ranges from $i = 2, 3, 4, \ldots, (p+1)$. Here, $(p+1)$ is the number of node points in the 1-D Legendre spectral finite element. As mentioned earlier, one of the main drawbacks of the finite elements formulated under Lagrangian frame of reference is the presence of zero energy modes. The number of these zero energy modes increase as the mesh is refined in the Lagrangian finite element model, and as the polynomial order (p) of the element shape function is increased in the Legendre spectral finite element model. Hamdi et al. [15] applied the rotational constraint on the fluid element to convert these zero energy modes into high order rotational modes. In the next two subsections, we will explore the behaviour of these spectral finite elements with respect to the quadrature schemes employed (*GLL, GL*) to evaluate the finite element matrices in Eq. (14).

3.1.1. GLL-quadrature scheme for both volumetric and rotational stiffness matrices

As explained in Section 2, $(p+1) \times (p+1)$ *GLL* quadrature can be employed on both the stiffness and the mass matrices. The obtained modes from the finite element analysis are given in Table 1. For the finite element discretization, single Legendre spectral finite element with polynomial order $p = 2$ is used. Hence for this element model, 3×3 *GLL* quadrature on both the stiffness and the mass matrices is employed. The authors, Hamdi et al. [15], Gopalakrishnan [10] and Kishor et al. [11] showed that the Lagrangian finite element formulation results in large number of spurious modes in addition to the zero energy modes, which are difficult to determine by mere inspection. By prescribing irrotationality condition on the displacement field, the zero energy or circulation modes vanish. This constraint is taken into account by a penalty method. The selection of a large constraint parameter will cause the rotation or vorticity associated with the fluid to go to zero and this in turn causes the strain energy associated with the rotation to approach zero. Here, we employ different numerical integration order on the rotational stiffness matrix given in Eq. (15) to make it rank deficient to see that the zero energy modes are eliminated from the finite element solution without stiffening the element. In the following analysis, we employ $(p+1) \times (p+1)$ *GLL* quadrature on the volumetric stiffness and the mass matrices, and vary the *GLL* quadrature order on the rotational stiffness matrix.

Since, (1×1) *GLL* quadrature scheme does not exist, first (2×2) *GLL* quadrature is employed on the rotational stiffness matrix and solved the eigenvalue problem (Eq. (13)) to study the behaviour of the zero energy modes with increase in the value of rotational constraint parameter R. As the value of R is increased from $0K$ to $1000K$, one zero energy mode is obtained. One slosh mode is present till $R = 10^{-6}K$, beyond this value of R, the slosh mode disappears and converts itself into a spurious mode. The remaining modes will be either acoustic or rotational modes. As the order of the *GLL*-quadrature on the rotational stiffness matrix is increased further to (3×3), zero energy modes which were present in the previous case are removed. The behaviour of the slosh modes with increase in the value of R is similar to the previous element model.

In Table 2, we give different mode count generated from the Legendre spectral element with polynomial order $p = 3$. From Section 2, it is clear that this element requires (4×4) *GLL* quadrature on both finite element stiffness and mass matrices. First, (2×2) *GLL* quadrature is employed on the rotational stiffness matrix, which gives four zero energy modes for the given range of R. The two slosh modes, which were present at $R = 0K$ reduces to 0 at $R = 10^{-5}K$. With (3×3) *GLL* quadrature four zero energy modes, which were associated with previous element model, now reduces to one. The pattern of number of slosh modes obtained with present element model is similar to that of $I_v = (4 \times 4)$ and $I_r = (2 \times 2)$ element model.

From the above two tables, it is clearly understood that the two Legendre spectral finite elements with $p = 2$ and $p = 3$ are unable to either remove the zero energy or the spurious modes, in addition to not capturing the slosh modes. In the present analysis, we increased the *GLL* quadrature order on the rotational stiffness matrix, from (2×2) to (3×3) to study the effect

Table 1
Mode count for polynomial order $p = 2$, and number of element $n = 1$, with *GLL*-quadrature on both volumetric and rotational stiffness matrix.

I_v	I_r	R	N_z	N_{sl}	N_a	N_r	N_m	I_r	N_z	N_{sl}	N_a	N_r	N_m	N_t
3×3	2×2	$0K$	1	1	7	0	0	3×3	1	1	7	0	0	9
3×3	2×2	$10^{-8}K$	1	1	7	0	0	3×3	1	1	7	0	0	9
3×3	2×2	$10^{-7}K$	1	1	7	0	0	3×3	0	1	7	1	0	9
3×3	2×2	$10^{-6}K$	1	1	7	0	0	3×3	0	1	7	1	0	9
3×3	2×2	$10^{-5}K$	1	0	7	0	1	3×3	0	1	7	1	0	9
3×3	2×2	$10^{-4}K$	1	0	7	0	1	3×3	0	0	7	1	1	9
3×3	2×2	$10^{-3}K$	1	0	7	1	0	3×3	0	0	7	1	1	9
3×3	2×2	$10^{-2}K$	1	0	7	1	0	3×3	0	0	7	2	0	9
3×3	2×2	$10^{-1}K$	1	0	7	1	0	3×3	0	0	6	2	1	9
3×3	2×2	$10^{-0}K$	1	0	5	0	3	3×3	0	0	3	1	5	9
3×3	2×2	$10^{+1}K$	1	0	4	0	4	3×3	0	0	2	1	6	9
3×3	2×2	$10^{+2}K$	1	0	6	2	0	3×3	0	0	1	2	6	9
3×3	2×2	$10^{+3}K$	1	0	6	2	0	3×3	0	0	3	6	0	9

Note: I_v = integration order of volumetric stiffness matrix, I_r = integration order of rotational stiffness matrix, N_z = number of zero energy modes, N_{sl} = number of slosh modes, N_a = number of acoustic modes, N_r = number of rotational modes, N_m = number of mixed modes, N_t = total number of modes.

Table 2
Mode count for polynomial order $p = 3$, and number of element $n = 1$, with *GLL*-quadrature on both volumetric and rotational stiffness matrix.

I_v	I_r	R	N_z	N_{sl}	N_a	N_r	N_m	I_r	N_z	N_{sl}	N_a	N_r	N_m	N_t
4×4	2×2	$0K$	4	2	14	0	0	3×3	4	2	14	0	0	20
4×4	2×2	$10^{-8}K$	4	2	14	0	0	3×3	4	2	14	0	0	20
4×4	2×2	$10^{-7}K$	4	2	14	0	0	3×3	3	2	14	1	0	20
4×4	2×2	$10^{-6}K$	4	1	14	0	1	3×3	1	2	14	2	1	20
4×4	2×2	$10^{-5}K$	4	0	14	0	2	3×3	1	1	14	2	2	20
4×4	2×2	$10^{-4}K$	4	0	14	1	1	3×3	1	0	14	3	2	20
4×4	2×2	$10^{-3}K$	4	0	14	2	0	3×3	1	0	14	4	1	20
4×4	2×2	$10^{-2}K$	4	0	14	2	0	3×3	1	0	13	5	9	20
4×4	2×2	$10^{-1}K$	4	0	12	1	3	3×3	1	0	12	4	3	20
4×4	2×2	$10^{-0}K$	4	0	10	0	6	3×3	1	0	8	2	9	20
4×4	2×2	$10^{+1}K$	4	0	14	1	1	3×3	1	0	7	2	10	20
4×4	2×2	$10^{+2}K$	4	0	14	2	0	3×3	1	0	12	6	1	20
4×4	2×2	$10^{+3}K$	4	0	14	2	0	3×3	1	0	12	7	0	20

Note: I_v = integration order of volumetric stiffness matrix, I_r = integration order of rotational stiffness matrix, N_z = number of zero energy modes, N_{sl} = number of slosh modes, N_a = number of acoustic modes, N_r = number of rotational modes, N_m = number of mixed modes, N_t = total number of modes.

of the rotational constraint on the element behaviour. The Legendre spectral finite element with polynomial order $p = 2$ and (3×3) *GLL* quadrature on the rotational stiffness shows the ability of predicting one slosh mode which is a fundamental mode, without generating zero energy modes for very small values of R. However, as the value of R is increased this slosh mode disappear as given in Table 1. But, when the polynomial order (p) is increased to 3, and with (3×3) *GLL* quadrature on the rotational stiffness matrix, two slosh modes are captured for very small values of R. When R is increased these slosh modes disappear. At the same time, one zero energy mode is appeared for the given range of R as given in Table 2, and the number of this zero energy mode increases as the mesh is refined.

From the above analysis, it is clearly seen that the rotational constraint applied in Eq. (7) is not effective in removing all the zero energy modes. In addition, the rotational constraint with the *GLL*-quadrature altered some of the slosh modes and converted them into mixed or spurious modes. The goal of the present paper is to eliminate all the zero energy modes, without altering the accuracy of the slosh and acoustic modes.

3.1.2. GLL-quadrature scheme for the volumetric and Gauss–Legendre quadrature scheme for the rotational stiffness matrix

It is observed in the previous section that the zero energy modes appear in the Legendre spectral finite element model in spite of enforcing the rotational constraint on the fluid element model using the *GLL* quadrature, and it did not capture the slosh modes. This can be explained as, increase in the integration order increases the number of constraints to be satisfied. If the constraint count, which is the ratio of number of active degrees of freedom to the number of constraints (number of integration points), becomes less than or equal to one, then the element locks severely [40]. Note that each integration point has to satisfy two constraints in the present element, namely incompressibility and irrotationality constraints. For the Legendre spectral element with shape function polynomial order p, there are $(p+1)$ nodes and $(p+1)$ integration points in 1-D, and in 2-D we have $(p+1)\times(p+1)$ nodes and integration points, respectively. The total number of active degrees of freedom in 2-D element is $2(p+1)^2$. The number of *GLL* integration points required for evaluation of the volumetric and the rotational stiffness matrices will be $(p+1)^2$, respectively. Hence the constraint count

$$C_c = \frac{\text{Active degrees of freedom}}{\text{Total number of constraints}} = \frac{2(p+1)^2}{2(p+1)^2} = 1.$$

So, the formulated spectral element with the *GLL* quadrature on both the stiffness and the mass matrices will lock. The performance of the element can be improved if we reduce the number of constraints, or in other words reduce the number of integration points. Here, we explain how to reduce the number of integration points in the finite element. Since the rotational constraint is a weak constraint, we can integrate the rotational stiffness matrix by a very small order quadrature rule, which is just sufficient to convert the circulation modes to rotational modes without making the slosh modes to alter. However, using the *GLL* quadrature, we cannot reduce the integration order below (2×2). Here, we propose a new procedure where in the volumetric stiffness and mass matrices are integrated using $(p+1)\times(p+1)$ *GLL* quadrature, and for the rotational stiffness matrix, one can use the *Gauss–Legendre* (*GL*) quadrature. Such a procedure offer tremendous flexibility in choosing appropriate integration order so that twin objectives of eliminating the zero energy and mixed or spurious modes. The results and appropriate *Gauss–Legendre* quadrature rule are given in Tables 3 and 4 for different values of rotational modulus R.

Table 3 gives the different mode count obtained with the Legendre spectral finite element having interpolation polynomial order $p = 2$. The numerical integration order required on these finite element matrices is (3×3) *GLL* quadrature. It is observed in the last section that the slosh modes are not captured from the finite element model with the above mentioned

Table 3
Mode count for polynomial order $p = 2$, and number of element $n = 1$, *GLL*-quadrature on volumetric and *Gauss–Legendre* quadrature on rotational stiffness matrix.

I_v	I_r	R	N_z	N_{sl}	N_a	N_r	N_m	I_r	N_z	N_{sl}	N_a	N_r	N_m	N_t
3×3	0×0	$10^{-9}K$	1	1	7	0	0	0×0	1	1	7	0	0	9
3×3	1×1	$10^{-8}K$	1	1	7	0	0	2×2	1	1	7	0	0	9
3×3	1×1	$10^{-7}K$	0	1	7	1	0	2×2	0	1	7	1	0	9
3×3	1×1	$10^{-6}K$	0	1	7	1	0	2×2	0	1	7	1	0	9
3×3	1×1	$10^{-5}K$	0	1	7	1	0	2×2	0	1	7	1	0	9
3×3	1×1	$10^{-4}K$	0	1	7	1	0	2×2	0	0	7	1	1	9
3×3	1×1	$10^{-3}K$	0	1	7	1	0	2×2	0	0	7	1	1	9
3×3	1×1	$10^{-2}K$	0	1	7	1	0	2×2	0	0	7	2	0	9
3×3	1×1	$10^{-1}K$	0	1	7	1	0	2×2	0	0	6	1	2	9
3×3	1×1	$10^{-0}K$	0	1	7	1	0	2×2	0	0	3	0	6	9
3×3	1×1	$10^{+1}K$	0	1	7	1	0	2×2	0	0	4	1	4	9
3×3	1×1	$10^{+2}K$	0	1	7	1	0	2×2	0	0	5	1	3	9
3×3	1×1	$10^{+3}K$	0	1	7	1	0	2×2	0	0	5	4	0	9

Note: I_v = integration order of volumetric stiffness matrix, I_r = integration order of rotational stiffness matrix, N_z = number of zero energy modes, N_{sl} = number of slosh modes, N_a = number of acoustic modes, N_r = number of rotational modes, N_m = number of mixed modes, N_t = total number of modes.

Table 4
Mode count for polynomial order $p = 3$, and number of element $n = 1$, *GLL*-quadrature on volumetric and *Gauss–Legendre* quadrature on rotational stiffness matrix.

I_v	I_r	R	N_z	N_{sl}	N_a	N_r	N_m	I_r	N_z	N_{sl}	N_a	N_r	N_m	N_t
4×4	0×0	$10^{-9}K$	4	2	14	0	0	0×0	4	2	14	0	0	20
4×4	1×1	$10^{-8}K$	4	2	14	0	0	2×2	4	2	14	0	0	20
4×4	1×1	$10^{-7}K$	4	2	14	0	0	2×2	0	2	14	4	0	20
4×4	1×1	$10^{-6}K$	3	2	14	1	0	2×2	0	2	14	4	0	20
4×4	1×1	$10^{-5}K$	3	2	14	1	0	2×2	0	2	14	4	0	20
4×4	1×1	$10^{-4}K$	3	2	14	1	0	2×2	0	2	14	4	0	20
4×4	1×1	$10^{-3}K$	3	2	14	1	0	2×2	0	2	14	4	0	20
4×4	1×1	$10^{-2}K$	3	2	14	1	0	2×2	0	2	14	4	0	20
4×4	1×1	$10^{-1}K$	3	2	14	1	0	2×2	0	2	13	4	1	20
4×4	1×1	$10^{-0}K$	3	2	14	0	2	2×2	0	2	11	1	6	20
4×4	1×1	$10^{+1}K$	3	2	14	1	0	2×2	0	2	13	3	2	20
4×4	1×1	$10^{+2}K$	3	2	14	1	0	2×2	0	2	14	4	0	20
4×4	1×1	$10^{+3}K$	3	2	14	1	0	2×2	0	2	14	4	0	20

Note: I_v = integration order of volumetric stiffness matrix, I_r = integration order of rotational stiffness matrix, N_z = number of zero energy modes, N_{sl} = number of slosh modes, N_a = number of acoustic modes, N_r = number of rotational modes, N_m = number of mixed modes, N_t = total number of modes.

quadrature scheme. Here, we apply a different quadrature rule to integrate the stiffness matrices. As stated earlier, we use the standard *GLL* quadrature on the volumetric stiffness and the mass matrices and *Gauss–Legendre* quadrature on the rotational stiffness matrix. Here, we fix the *GLL* quadrature on the volumetric stiffness and mass matrices and varied the *Gauss–Legendre* quadrature on the rotational stiffness matrix, to see the objective of eliminating the zero energy and mixed modes is achieved. In the *Gauss–Legendre* quadrature the integration order starts from 1. This (1×1) *Gauss–Legendre* quadrature is employed in the present spectral element to evaluate the rotational stiffness matrix and (3×3) *GLL* quadrature is employed to evaluate the volumetric stiffness matrix. Interestingly, all the zero energy modes which are present at $R = 0K$ are eliminated for higher values of R. In addition to that, one slosh mode is captured. The remaining modes are acoustic and rotational modes. To investigate further the effect of *Gauss–Legendre* quadrature on the rotational stiffness, (2×2) *Gauss–Legendre* quadrature is used on the rotational stiffness matrix. The different modes obtained using the above quadrature is also given in Table 3. With this element model also, the single zero energy mode which is present at $R = 0K$ is eliminated for higher values of R. However, the slosh mode, which is present at $R = 0K$, disappears for values of R greater than $R = 10^{-5}K$. Hence, it is clear that, for a Legendre spectral finite element with interpolation polynomial order $p = 2$, (1×1) *Gauss–Legendre* quadrature is appropriate on the rotational stiffness.

In the next experiment, the polynomial order (p) of the element shape function is increased and calculated different modes as done with the previous element model. Table 4 gives the different mode count generated from the Legendre spectral finite element with shape function polynomial order $p = 3$. When (1×1) *Gauss–Legendre* quadrature is employed on the rotational stiffness matrix, four zero energy, two slosh and 14 acoustic modes are obtained when $R = 0K$. As the

value of R is increased to $R = 10^{-6}K$, four zero energy modes reduced to three and the two slosh modes remain constant till $R = 10^{3}K$. The remaining modes are either acoustic or rotational or mixed modes. For (2×2) *Gauss–Legendre* quadrature on the rotational stiffness, we get no zero energy modes for higher values of rotational modulus ($R > 10^{-8}$), and the two slosh modes obtained at $R = 0K$ does not change with R. The remaining modes are either acoustic or rotational or mixed modes.

From the above analysis, two aspects are clear. The *Gauss–Legendre* quadrature not only eliminates all the zero energy modes, but also completely eliminates the mixed or spurious modes for higher values of rotational modulus *i.e.*, when $R = 10^{3}K$. In addition, the number of slosh, rotational and acoustic modes captured follows a specific pattern. If the total number of modes in the finite element model is N_t, then the number of slosh modes is equal to $N_{sl} = (p-1)$, the number of rotational modes is $N_r = (p-1)^2$ and the number of acoustic modes is $N_{ac} = N_t - N_{sl} - N_r$, with $(p+1) \times (p+1)$ *GLL* quadrature on the volumetric stiffness and mass matrix and $(p-1) \times (p-1)$ *Gauss–Legendre* quadrature on the rotational stiffness matrix.

Table 5 summarizes the numerical results obtained from the spectral finite element solution for various polynomial orders of p. For $p = 1$ we get no slosh mode, and for $p = 7$ we get six slosh modes. As the polynomial order p is increased, the finite element solution approaches the exact solution. This is clearly observed in Table 5. We can also see that if the Legendre element polynomial order is p, we get $(p-1)$ low frequency slosh modes. In the above all calculations, we discretized the fluid system with only one element and used $(p+1) \times (p+1)$ *GLL* quadrature on the volumetric stiffness and mass matrices, and $(p-1) \times (p-1)$ *Gauss–Legendre* quadrature on the rotational stiffness matrix. The above analysis shows that the proposed spectral element with the *GLL* quadrature on the volumetric stiffness and the mass matrices, and the *Gauss–Legendre* quadrature on the rotational stiffness matrix, not only eliminates the zero energy and mixed modes, but also captures the acoustic and slosh modes accurately.

3.2. The inf–sup test

The performance of the newly formulated Legendre spectral elements under twin constraints: namely incompressibility and irrotationality is assessed using the inf–sup test. The inf–sup test is similar to the patch test and is used to test the performance of the element behaviour. The inf–sup test takes into account the mesh density, mesh distortion, integration order on the constrained matrices and the boundary conditions, and does not take into account the applied loading like the patch test.

This test essentially transforms the naturally occurring constrained strain fields into an eigenvalue problem given by

Table 5
First few slosh and acoustic frequencies for various polynomial orders of p with number of element $n = 1$.

Polynomial order (p)	Present method (ω_S) (rad/s)	Error (%)	Present method (ω_a) (rad/s)	Error (%)
$p = 1$			1168.1	1.4926
			2269.7	53.130
$p = 2$	2.0691	7.56	1183.60	0.1855
			1429.2	3.5757
$p = 3$	2.2480	0.424	1186.3	0.0421
	3.1882	7.5991	1486.2	0.2698
			1952.0	8.6869
$p = 4$	2.2380	0.0223	1186.3	0.0421
	3.4845	0.9882	1482.7	0.0337
	3.9251	7.8679	2176.8	1.8290
$p = 5$	2.2386	0.00446	1186.3	0.0421
	3.4402	0.2956	1482.9	0.0472
	4.3404	1.8801	2130.9	0.3180
	4.5514	7.5519	3558.9	0.0506
$p = 6$	2.2386	0.00446	1186.3	0.0421
	3.4506	0.00579	1485.6	0.0472
	4.2123	1.1266	2139.0	0.0608
	5.0895	3.3778	3559.0	0.0534
	5.1799	5.9367	3668.6	0.0518
$p = 7$	2.2386	0.00446	1186.3	0.0421
	3.4504	0	1482.9	0.0472
	4.2615	0.0281	2138.7	0.0467
	4.8020	2.4618	3559.0	0.0534
	5.7961	5.2936	3668.6	0.0518
	5.8421	3.1321		

Note: ω_S = slosh frequency, ω_a = acoustic frequency.

$$[\mathbf{G}]\{\phi\} = \lambda[\mathbf{S}]\{\phi\},$$

$$[\mathbf{G}] = \int_\Omega B_V^T B_V \, d\Omega + \int_\Omega B_R^T B_R \, d\Omega,$$

where B_V is the strain displacement matrix of the volumetric strain and B_R is the strain displacement matrix of the rotational strain, and $[\mathbf{S}]$ is given by

$$[\mathbf{S}] = \int_\Omega \left[\left(\frac{\partial u}{\partial x}\right)^2 + \left(\frac{\partial u}{\partial y}\right)^2 + \left(\frac{\partial v}{\partial x}\right)^2 + \left(\frac{\partial v}{\partial y}\right)^2 \right] d\Omega. \tag{25}$$

The inf–sup value λ is found from this eigenvalue problem, by taking the first non-zero eigenvalue of the system. For a given element, the inf–sup value is obtained for various mesh configurations; if this value does not change significantly for various mesh configurations then the element is said to have passed the test. This test is a critical requirement that any newly formulated element has to satisfy, however not satisfying this requirement is also acceptable for some elements [35].

The inf–sup test is first applied to the formulated Legendre spectral finite element with $p = 2$. It is observed from Section 3.1.1 and from Table 1, that this element model with (2×2) and (3×3) *GLL* quadrature on the rotational stiffness matrix did not predict the slosh modes and in the former case, zero energy modes were present. The inf–sup test results corresponding to this element are shown in Fig. 2(a). It is clear from the figure that the inf–sup value decreases as the mesh is refined. In the present study, we considered four mesh refinements. Fig. 2(b) shows the inf–sup test results of the spectral element with polynomial order $p = 3$ and (2×2), (3×3) *GLL* quadrature on the rotational stiffness matrix. The corresponding mode count obtained from this element model are given in Table 2. From this table, it is clear that all the zero energy modes are not eliminated as well as the slosh modes are not captured at all. The inf–sup value of this element model also decreases as the mesh is refined. Clearly, from the above study, these two element models do not satisfy the inf–sup test and reinforces our earlier argument that these elements behave badly in predicting the slosh modes accurately.

In Section 3.1.2, we have used a different quadrature scheme to integrate the rotational stiffness and derived a relation between the interpolation polynomial order p of the element shape function and the *Gauss–Legendre* integration order which, when used on the rotational stiffness matrix predicted accurate results. With this relation, we could remove all the zero energy modes and the predicted slosh modes were very accurate. Here, we apply the inf–sup test to these newly formulated elements. From the relation given in Section 3.1.2, if the interpolation polynomial order is p, then we require $(p-1) \times (p-1)$ *Gauss–Legendre* quadrature on the rotational stiffness. Fig. 3(a) shows the inf–sup test results for the polynomial orders $p = 2, 3$ with (1×1) and (2×2) *Gauss–Legendre* quadrature on the rotational stiffness matrix respectively. The calculated inf–sup values does not change significantly as the mesh is refined and we say that these two element models pass the inf–sup test. However, if the *Gauss–Legendre* quadrature on the rotational stiffness is increased beyond the value given by the relation, which is given in Section 3.1.2, again the element behaved very badly. This undesired behaviour is seen in Tables 3 and 4 and in Fig. 3(b).

The results of the inf–sup test clearly suggest the superiority of the elements that used *GLL*-quadrature on the volumetric stiffness and on the mass matrix, and *Gauss–Legendre* quadrature on the rotational stiffness. We study convergence of these Legendre spectral finite elements, and use these elements to solve some special problems in the following sections.

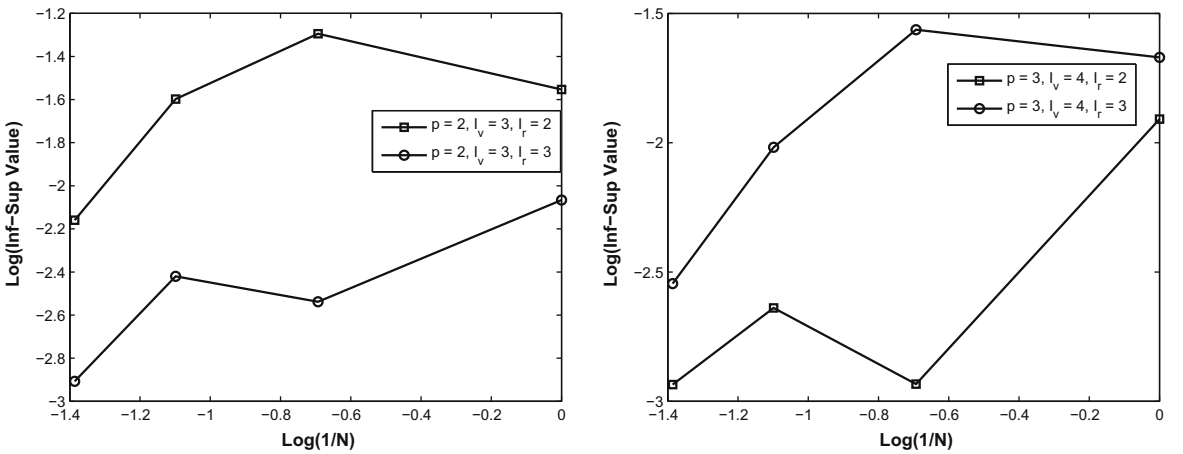

(a) Polynomial order p=2 (b) Polynomial order p=3

Fig. 2. Inf–sup test results for spectral element with GLL-quadrature rule on both volumetric and rotational stiffness matrices.

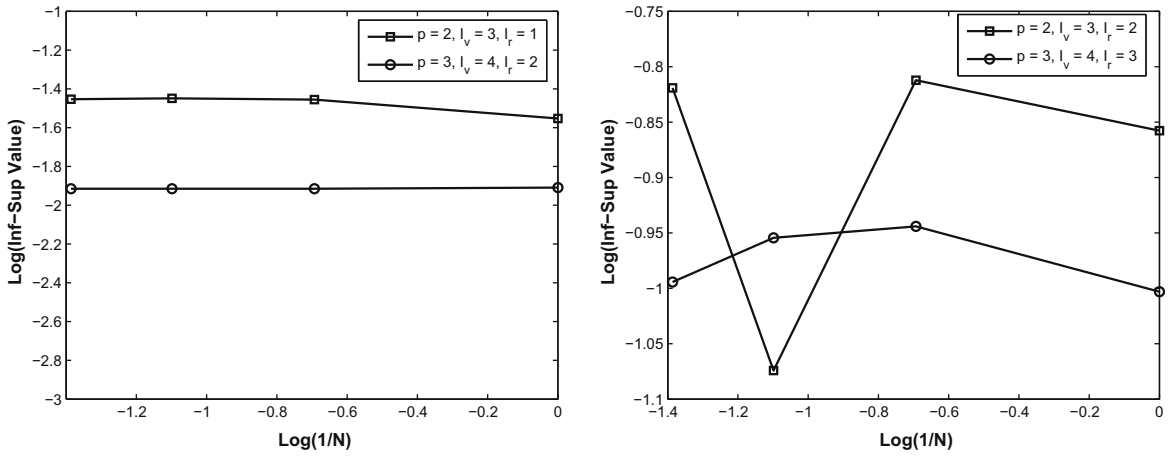

(a) Polynomial order p=2, 3 (b) Polynomial order p=2, 3

Fig. 3. Inf–Sup test results for spectral element with GLL-quadrature rule volumetric and *Gauss–Legendre* quadrature rule rotational stiffness matrix.

3.3. Convergence of the Legendre spectral element

The newly formulated spectral elements performance is analyzed in the present section by studying its convergence rates. In Fig. 4, comparison of errors in the slosh frequencies obtained by the *h*-type and the Legendre spectral elements is given. For the *h*-type finite element [10], we used linear Lagrange interpolation polynomial with $p = 1$, and full *Gauss–Legendre* quadrature as dictated by the polynomial order (p) is employed in evaluating the stiffness and mass matrices [6,10]. The number of degrees of freedom in the *h*-type finite element model is increased by increasing the number of elements whereas, in the Legendre spectral finite element model, the number of degrees of freedom is increased by increasing the polynomial order p of the element shape function keeping the number of elements constant. Here, we used only one Legendre spectral element to model the fluid, and increased the polynomial order (p) of the element shape function. For the comparison, the Legendre spectral element formulated in Section 3.1.2 is used to calculate the slosh and acoustic frequencies. The error ε is given by

$$\varepsilon = \frac{|\omega_{sl} - \tilde{\omega}_{sl}|}{|\tilde{\omega}_{sl}|},$$

where $\tilde{\omega}$ denotes the exact value. From Fig. 4, we see the exponential convergence for the spectral finite element solution in predicting the slosh modes, whereas the *h*-type finite element solution does not improve with increase in the number of degrees of freedom. This behaviour of *h*-type finite elements is also known as numerical locking in the incompressible limit. We see that the *h*-type finite element with full *Gauss–Legendre* quadrature do not capture the low frequency slosh modes [10,11]. The authors in [10,11] introduced reduced order *Gauss–Legendre* quadrature and the consistent formulation on

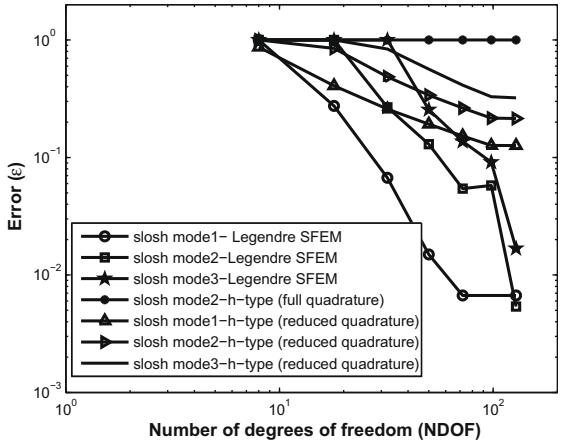

Fig. 4. Error of first three slosh frequencies.

the constrained strain fields to remove locking in the incompressible medium. The convergence rates of these locking free *h*-type finite elements are also given in Fig. 4. While using the locking free *h*-type finite elements, (1×1) *Gauss–Legendre* quadrature is employed on both the volumetric and the rotational stiffness matrices, whereas, (2×2) *Gauss–Legendre* quadrature is employed on the mass matrix. Fig. 4 clearly shows that the Legendre spectral element solution converges exponentially whereas, reduced quadrature *h*-type finite element solution shows *algebraic* convergence.

Fig. 5 shows the convergence rates in the acoustic modes. The same Legendre spectral element formulated in Section 3.1.2 is used for the present analysis also. In the case of *h*-type finite elements, full and reduced *Gauss–Legendre* quadrature on the volumetric and the rotational stiffness matrices yielded similar convergence rates, here only reduced quadrature results are shown in Fig. 5 to avoid clutter. From Fig. 5, the Legendre spectral elements shows faster convergence rates comparative to the *h*-type elements. In the above all results we have employed $(p+1) \times (p+1)$ *GLL* quadrature to evaluate the volumetric stiffness and the mass matrices whereas, $(p-1) \times (p-1)$ *Gauss–Legendre* quadrature on the rotational stiffness matrix for

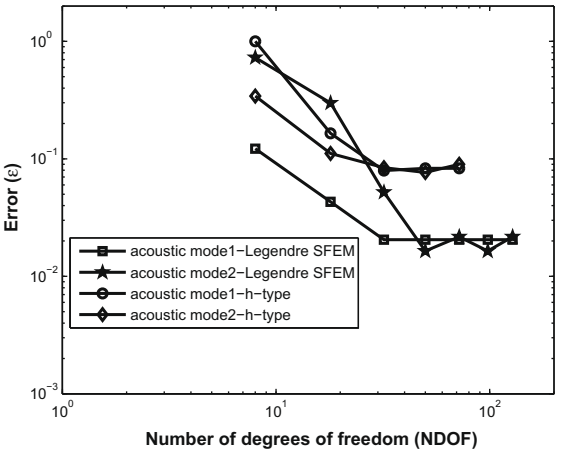

Fig. 5. Error of first two acoustic frequencies.

Table 6
First slosh frequency for various interpolation polynomial orders (p) with two undistorted and distorted spectral elements.

Polynomial order (p)	Exact (rad/s)	Undistorted element (rad/s)	Distorted (b_1 = 3.0 m) (rad/s)	% deviation
p = 2	2.2385	2.2337	2.6891	20
p = 3	2.2385	2.2386	2.3215	3.7
p = 4	2.2385	2.2386	2.2421	0.1
p = 5	2.2385	2.2386	2.2386	0.004

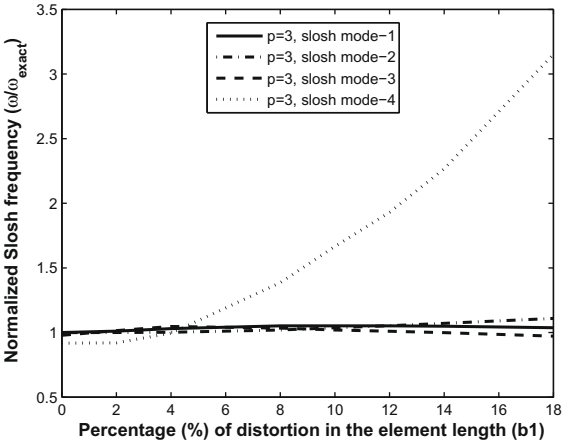

Fig. 6. Behaviour of slosh frequencies as a function of distorted element length b_1, for p = 3.

the Legendre spectral finite element model. From the above convergence studies, it can be said that the Legendre spectral element solution converges exponentially for smooth solutions.

3.4. Spectral element behaviour with distorted element mesh

The effect of geometric distortion and polynomial order (p) of the Legendre spectral element on the slosh frequencies is studied in the present section. First, for a set value of distorted element, behaviour of the slosh mode is studied for increasing value of element polynomial order (p). The distorted finite element model is shown in Fig. 1(b); with $b_1 = 3.0$ m, and this comes to 18% distortion of the actual single element length ($b/2$) in the tank model. The calculated slosh frequencies for various values of interpolation polynomial order (p) of the spectral element are given in Table 6. From the above analysis, it is understood that as the polynomial order (p) of the distorted element is increased, the stiffness is estimated more closely to the undistorted element and this in turn leads the obtained results to move close to the exact and undistorted element results. In the second experiment, for a set value of element polynomial order ($p = 3, 4$), behaviour of the slosh modes is studied for different values of distorted element length (b_1). From the finite element solution with $p = 3$, we get four slosh modes. The normalized slosh frequencies with exact results are given in Fig. 6. The percentage of distortion considered in the ele-

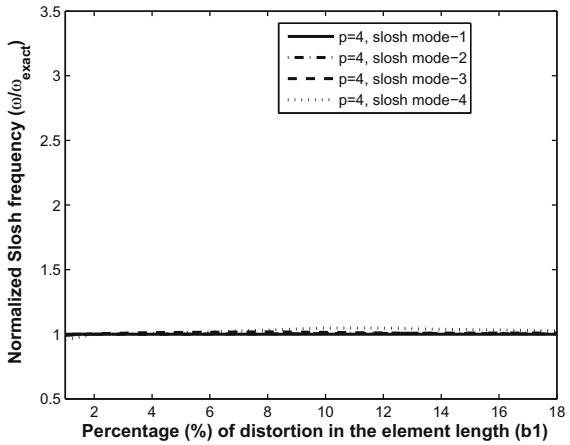

Fig. 7. Behaviour of slosh frequencies as a function of distorted element length b_1, for $p = 4$.

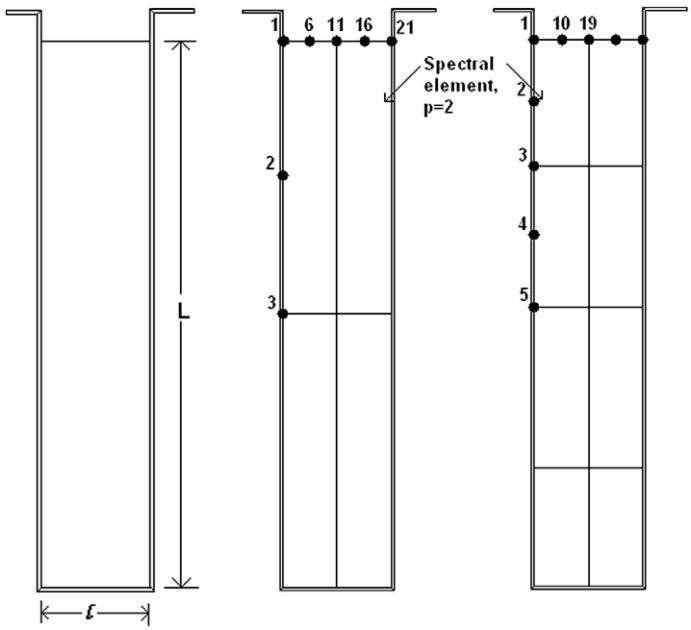

Fig. 8. Tall water column problem and its finite element discretization, $l = 0.0508$ m, $L = 0.508$ m, $K = 2.18 \times 10^9$ Pa and $\rho = 999$ kg/m^2.

ment length b_1 is given on the abscissa. As the percentage of distortion in the Legendre spectral element is increased, first three slosh modes showed small deviation from the exact results, whereas, the higher slosh mode (slosh mode-4) became spurious. If the polynomial order p is increased to 4, we get six slosh modes. As shown in Fig. 7, deviation of first four slosh modes is very small as the percentage of distortion in the element length is increased. In this case also, the higher slosh mode (slosh mode-6) became spurious which is not shown here. From the above study, as the polynomial order of the element shape function (p) is increased, distortion in the element has small effect on the first few slosh modes.

3.5. Natural frequencies in a tall water column

The accuracy and robustness of the present Legendre spectral finite element formulation is studied by solving an eigenvalue problem associated with a tall water column. Bathe [12] has calculated the acoustic frequencies in a tall water column using the h-type finite elements he has developed in [12]. In the present paper, the authors want to model the same tall water column with the same properties considered in [12] and compare our finite element results with that of results obtained in [12] by Bathe. Fig. 8 shows the "tall water column problem" and the fluid properties considered are bulk modulus K is 2.18×10^9 Pa, density of the fluid ρ is 999 kg/m^3. The height of the column is much higher than its width and has a free surface (pressure = 0). The exact solution to this problem is given in Eq. (23) by Bathe [12].

Fig. 8 shows the finite element mesh used to model the tall water column. In the present study, we used Legendre spectral finite element with element shape function interpolation polynomial order $p = 2$. Here, the problem is modeled with one, four and eight Legendre spectral elements respectively. In the analysis done by Bathe [12], the tall water column problem was discretized with 8-noded h-type Lagrangian finite elements. Table 7 compares the analytical and the finite element re-

Table 7
Analytical and FE solutions of acoustic frequencies of a tall water column with full *GLL* quadrature rule on both volumetric and rotational stiffness matrices with $R = 100K$.

Mode#	Analytical solution	FE [12] (80-elem) (rad/s)	Present method (1-elem) (rad/s)	Present method (4-elem) (rad/s)	Present method (8-elem) (rad/s)
1	4566	4567	4557.2	4567.1	4567.7
2	13698	13760	12855	13507	13694
3	22830	22890	82222	22668	22700

Table 8
Effect of rotational modulus R on FE solutions of acoustic frequencies in a tall water column with full *GLL* quadrature rule on both volumetric and rotational stiffness matrices.

Mode#	Analytical solution (rad/s)	Present method (8-elem) $R = 10^{-5}K$	Present method (8-elem) $R = 10^{-2}K$	Present method (8-elem) $R = K$	Present method (8-elem) $R = 10^{2}K$
1	4566	142.22	4464.9	4567.7	4567.7
2	13698	167.80	4567.7	13694.0	13694.0
3	22830	184.48	5205.5	22700.0	22700.0

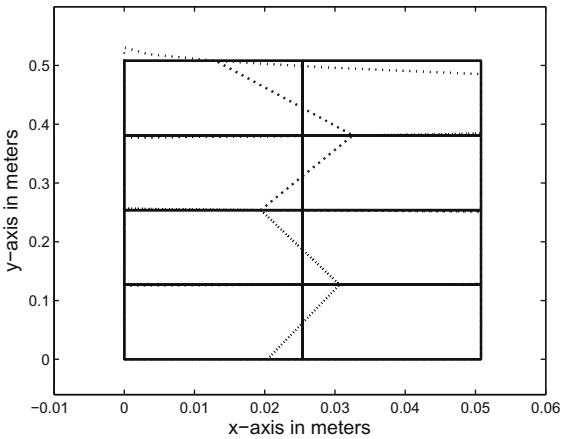

Fig. 9. Spurious acoustic mode-1 (142.22 rad/s), "..." shows mode shape and "–" shows initial geometry, with $R = 10^{-5}K$.

sults obtained from both the present formulation and Bathe's [12] formulation, which are in excellent agreement even for single element analysis. The tall water column problem allows us to examine the importance of the irrotationality parameter in the displacement-based finite element analysis of fluid frequencies. Table 8 shows the first three acoustic modes calculated by the formulated spectral finite element for different rotational modulus (R) on fluid particle rotations. Note that these modes do not represent physical modes for low rotational modulus ($R = 10^{-5}K$) as seen from Figs. 9–11.

As the rotational modulus (R) is increased to 100K, the acoustic modes tend to the exact values. These first three true acoustic mode shapes are shown in Figs. 12–14, and since gravity and sloshing motions are not included in the present analysis, the displacement patterns represent volume change patterns of the length of the tall water column [12–15].

3.6. Dynamic analysis of liquid partially filled in a rigid rectangular tank

In this section, we study the behaviour of the newly formulated Legendre spectral element in dynamic analysis. We consider a rigid rectangular tank partially filled with water having dimensions of $b = 0.9$ m and $h = 0.6$ m as the width and liquid height, respectively. The exact fundamental slosh frequency of this system is 5.75912 rad/s, and from the present finite element calculation with element polynomial order $p = 3$ and single element, it is 5.7639 rad/s. The finite element model is given in Fig. 15. The fluid system is subjected to a sinusoidal external acceleration as given below,

$$\ddot{x}(t) = -(x_0\omega^2)\sin(\omega t) \quad \text{for } t \geqslant 0,$$

where x_0 and ω are the amplitude and frequency of the forced sinusoidal displacement, respectively. The parameters x_0 and ω are taken as 0.002 and 5.5 rad/s, respectively [34]. These particular values have been considered to just compare our finite element formulation results with the already published standard test case results [34]. A time history analysis with linear, small deflection theory is carried out. The constant-average-acceleration Newmark time marching scheme with a time step

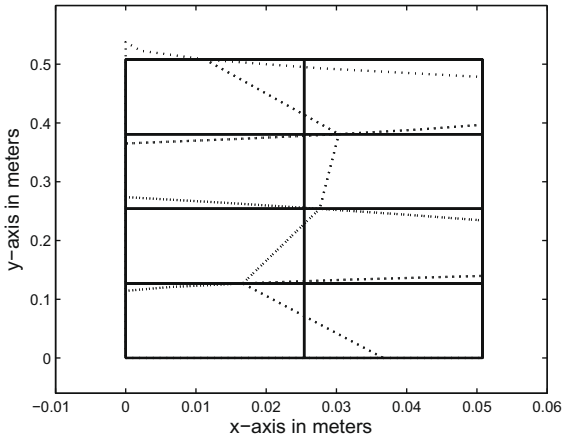

Fig. 10. Spurious acoustic mode-2 (167.80 rad/s), "..." shows mode shape and "–" shows initial geometry, with $R = 10^{-5}K$.

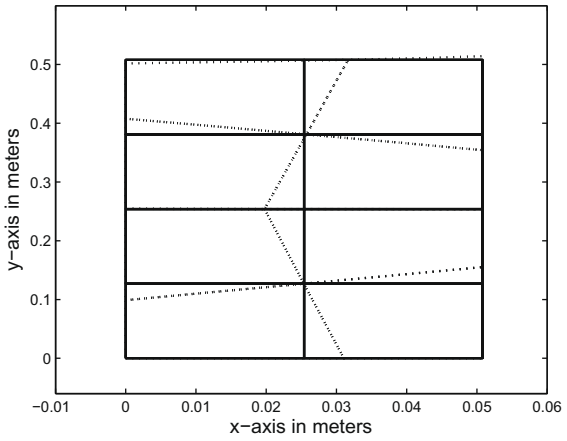

Fig. 11. Spurious acoustic mode-3 (184.48 rad/s), "..." shows mode shape and "–" shows initial geometry, with $R = 10^{-5}K$.

of $\Delta t = 0.02$ s is used. The computed free surface vertical displacements (sloshing wave height) for the tank is shown in Figs. 16 and 17. It is observed from Fig. 16 that the present Legendre spectral finite element results compare well with the Boundary element method (BEM) results of Nakayama et al. [34]. Since the sloshing motion is antisymmetric with respect to the

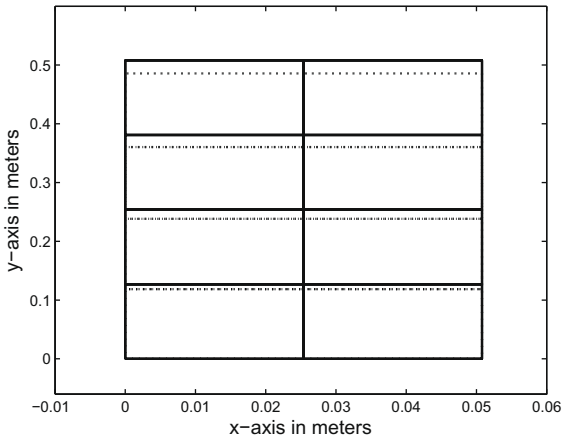

Fig. 12. True acoustic mode-1, $\omega = 4567.7$ rad/s, "..." shows mode shape and "–" shows initial geometry, with $R = 10^2 K$.

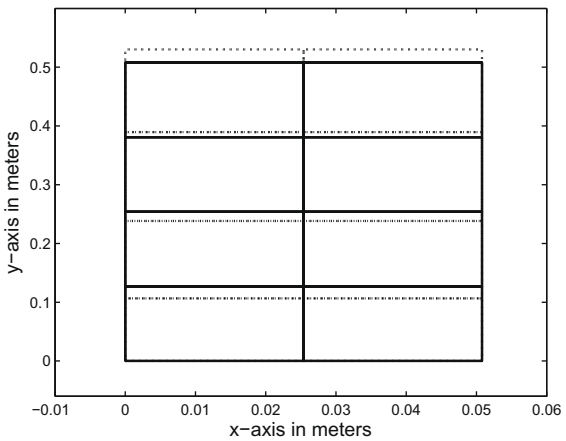

Fig. 13. True acoustic mode-2, $\omega = 13694$ rad/s, "..." shows mode shape and "–" shows initial geometry, with $R = 10^2 K$.

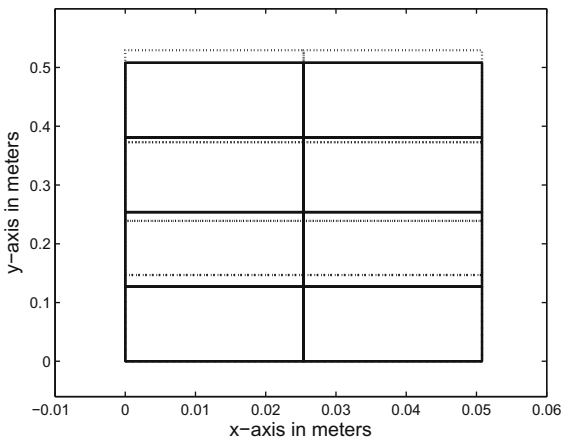

Fig. 14. True acoustic mode-3, $\omega = 22700$ rad/s, "..." shows mode shape and "–" shows initial geometry, with $R = 10^2 K$.

vertical symmetric axis, the free surface displacements at the left and right corner will be out of phase by 180°. From Fig. 17, it is observed that the free surface displacements at the left and right corners are exactly antisymmetric and maximum vertical displacements occurs at these points.

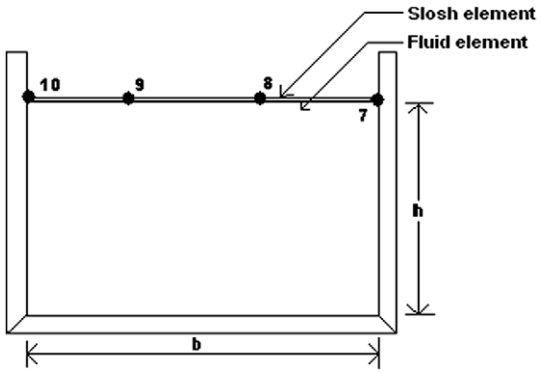

Fig. 15. 2-D finite element discretization of rectangular tank with $p = 3$ and $b = 0.9$ m, $h = 0.6$ m.

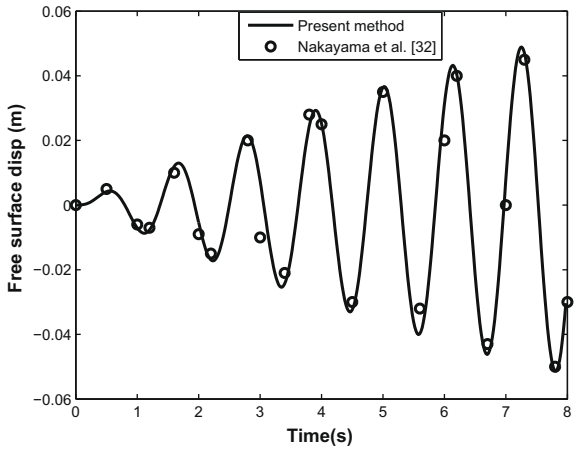

Fig. 16. Free surface vertical displacement near wall of the rectangular tank under sinusoidal base excitation, $\ddot{x} = -x_0\omega^2 \sin(\omega t)$, ($x_0 = 0.002$ m, $\omega = 5.5$ rad/s).

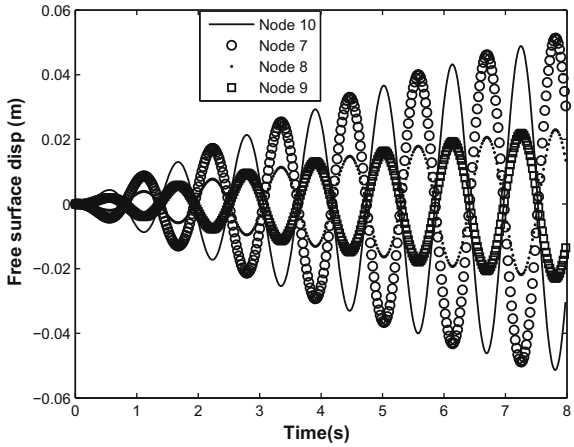

Fig. 17. Free surface vertical displacement at various points of the rectangular tank under sinusoidal base excitation, $\ddot{x} = -x_0\omega^2 \sin(\omega t)$, ($x_0 = 0.002$ m, $\omega = 5.5$ rad/s).

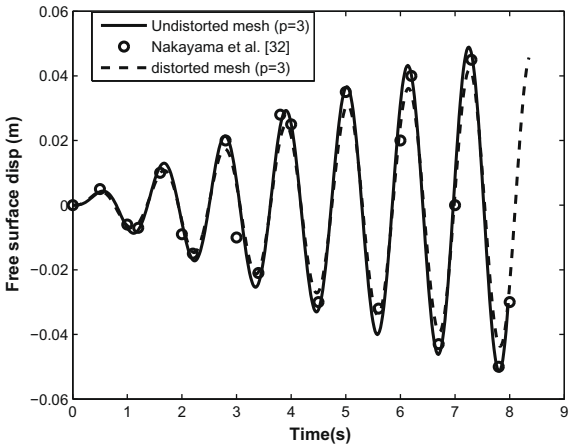

Fig. 18. Free surface vertical displacements near wall of rectangular tank under sinusoidal base excitation, $\ddot{x} = -x_0\omega^2 \sin(\omega t)$, ($x_0 = 0.002$ m, $\omega = 5.5$ rad/s), and $b = 0.9$ m, $b_1 = 0.5$ m and $h = 0.6$ m.

3.6.1. Dynamic analysis of liquid with distorted elements

In the present section, the formulated Legendre spectral element behaviour is studied with geometric distorted elements in the dynamic analysis. The considered distorted element shape function polynomial order p is 3. The distorted finite element model is given in Fig. 1(b); with $b = 0.9$ m, $h = 0.6$ m, and $b_1 = 0.50$ m this comes to 11% distortion of the actual single element length in the tank model. The comparison of slosh wave heights at the left corner of the rectangular tank between the undistorted and distorted elements with Nakayama et al. [34] results is given in Fig. 18. It is observed from Fig. 18, that the dynamic free surface heights obtained from the distorted elements with $p = 3$ follows the trend obtained with undistorted elements and with the Nakayama et al. [34] results. From the above study, we can say that the formulated element is also able to show good behaviour with distorted elements in dynamic analysis.

4. Conclusions

A Legendre spectral finite element model is developed to model the acoustic fluids to calculate the slosh and the acoustic modes in incompressible limit. Legendre spectral finite elements have their shape functions obtained by the Lagrangian interpolants with node locations at $(p+1)$ *GLL* points. Here, Legendre spectral finite element node locations and *GLL* quadrature point locations are coincident. For the Legendre spectral finite element volumetric stiffness and mass matrices, *Gauss–Lobatto–Legendre* (*GLL*) quadrature is used for the numerical integration, while for the rotational stiffness matrix, use of *Gauss–Legendre* (*GL*) quadrature gives superior results. The zero energy modes which are inherently present in the Legendre spectral finite element model are completely converted into high order rotational modes by reduced order *Gauss-Legendre quadrature* on the rotational stiffness matrix. From the present study, the ideal value of rotational parameter (R) will be between 10^2K and 10^4K for accurate slosh frequencies.

Comparison of natural frequencies obtained by the *h*-type finite elements and the Legendre spectral finite elements reveal that the spectral finite element solution is more accurate than the *h*-type finite element solution. Moreover, this Legendre spectral finite elements give exponential convergence rates. From the present analysis, we derived the following relation: if the fluid domain is modeled with an element having interpolation polynomial of order p, then the Legendre spectral finite element solution produces $(p-1)$ slosh modes, $(p-1)^2$ rotational modes and $N_t - (p-1) - (p-1)^2$ acoustic modes, where N_t is the total number of modes present in the finite element model. This specific pattern in different modes is achieved if the spectral element is integrated with $(p+1)\times(p+1)$ *GLL* quadrature on the volumetric stiffness and the mass matrices, and $(p-1)\times(p-1)$ *Gauss–Legendre* quadrature on the rotational stiffness matrix. Clearly, the formulated spectral elements with above mentioned quadrature rule satisfies the inf–sup test and are free of locking.

References

[1] H. Stolarski, T. Belytschk, Membrane locking and reduced integration for curved elements, Journal of Applied Mechanics 49 (1981) 172–178.
[2] G. Prathap, G.R. Bhashyam, Reduced integration and the shear flexible beam element, International Journal for Numerical Methods in Engineering 18 (1982) 195–210.
[3] H. Stolarski, T. Belytschko, Shear and membrane locking in curved C^0 elements, Computer Methods in Applied Mechanics and Engineering 41 (1983) 279–296.
[4] T. Belytschko, H. Stolarski, W.K. Liu, N. Carpenter, J.S.J. Ong, Stress projection for membrane and shear locking in shell finite elements, Computer Methods in Applied Mechanics and Engineering 51 (1985) 221–258.
[5] A.K. Noor, J.M. Peters, Mixed models and reduced/selective integration for curved beam elements, International Journal for Numerical Methods in Engineering 17 (1981) 615–631.

[6] R.D. Cook, D.S. Malkus, M.E. Plesha, R.J. Witt, Concepts and Applications of Finite Element Analysis, John Wiley & Sons, Inc., 2002.
[7] G. Prathap, Field consistent finite element formulations, Interner Bericht IB 131-84/33, DFVLR Institute fur Strukturmechanik, Braunschweig, W. Germany, 1984.
[8] G. Prathap, Field consistency and the finite element analysis of multi-field structural problems, in: K.A.V. Pandalai and B.R. Somashekar (Eds) , Analysis of Structures NAL-SP-RPT-1/84, Bangalore, 1984.
[9] C. Satish, G. Prathap, A field-consistent formulation for the eight noded solid finite element, Computers and Structures 2 (1989) 345–355.
[10] S. Gopalakrishnan, Behaviour of isoparametric quadrilateral family of Lagrangian fluid finite elements, International Journal for Numerical Methods in Engineering 54 (2001) 731–761.
[11] D.K. Kishor, S. Gopalakrishan, R. Ganguli, Three dimensional sloshing: a consistent finite element approach, International Journal for Numerical Methods in Fluids, in press.
[12] G.L. Olson, K.J. Bathe, A study of displacement based fluid finite elements for calculating frequencies of the fluid and fluid–structure systems, Nuclear Engineering and Design 76 (1983) 137–151.
[13] E.L. Wilson, M. Khalvathi, Finite elements for dynamic analysis of fluid–solid systems, International Journal for Numerical Methods in Engineering 19 (1983) 1657–1668.
[14] L. Kiefling, G.C. Feng, Fluid–structure finite element vibration analysis, AIAA Journal 41 (2) (1976) 199–203.
[15] M.A. Hamdi, T. Ousset, A displacement method of analysis of vibration of coupled fluid–structure system, International Journal for Numerical Methods in Engineering 13 (1978) 139–150.
[16] Y. Başar, U. Hanskötter, Ch. Schwab, A general high-order finite element formulation at large strains and finite rotations, International Journal for Numerical Methods in Engineering 57 (2003) 2147–2175.
[17] I. Babuška, M. Suri, The p and $h - p$ versions of the finite element method, basic principles and properties, SIAM Review 36 (1994) 578–632.
[18] G.E.M. Karniadakis, S. Sherwin, Spectral/*hp* Element Methods for Computational Fluid Dynamics, Oxford University Press, 2005.
[19] O.C. Zienkiewicz, R.L. Taylor, J.Z. Zhu, The Finite Element Method: Its Basis and Fundamentals, sixth ed., Butterworth-Heinemann, 2005.
[20] A.T. Patera, A spectral element method for fluid dynamics: laminar flow in a channel expansion, Journal of Computational Physics 54 (1984) 468–488.
[21] C. Canuto, M.Y. Hussaini, A. Quarteroni, T.A. Zang, Spectral Methods in Fluid Dynamics, Springer-Verlag, New York, 1998.
[22] D. Gottlieb, S.A. Orszag, Numerical Analysis of Spectral Methods: Theory and Applications, SIAM, Philadelphia, PA, 1977.
[23] M.O. Deville, P.F. Fischer, E.H. Mund, High-Order Methods for Incompressible Fluid Flow, Cambridge University Press, 2002.
[24] M.A. Sprague, T.L. Geers, Spectral elements and field separation for an acoustic fluid subject to caviation, Journal of Computational Physics 184 (2003) 149–162.
[25] D. Komatitsch, J.P. Vilotee, The spectral element method: an efficient tool to simulate the seismic response of 2D and 3D geological structures, Bulletin of the Seismological Society of America 88 (2) (1998) 368–392.
[26] D.S. Malkus, I. Fried, Finite element mass matrix lumping by numerical integration with no convergence rate loss, International Journal of Solids and Structures 11 (1975) 461–466.
[27] T.J.R. Hughes, The Finite Element Method Linear Static and Dynamic Finite Element Analysis, Prentice-Hall, Inc., 1987.
[28] B. Szabo, I. Babuska, Finite Element Analysis, Wiley, New York, 1991.
[29] J.H. Hommel, G. Meschke, EAS concept for higher-order finite shell elements to eliminate volumetric locking, International Journal for Numerical Methods in Engineering 75 (12) (2008) 1416–1434.
[30] M. Bischoff, E. Ramm, D. Braess, A class of equivalent enhanced assumed strain and hybrid stress finite elements, Computational Mechanics 22 (1999) 443–449.
[31] M.A. Sprague, T.L. Geers, Legendre spectral finite elements for structural dynamics analysis, Communications in Numerical Methods in Engineering 24 (2008) 1953–1965.
[32] E.M. Ronquist, A.T. Patera, A Legendre spectral element method for the Stefan problem, International Journal for Numerical Methods in Engineering 24 (1987) 2273–2299.
[33] J.M. Melenk, K. Gerdes, C. Schwab, Fully discrete hp-finite elements: fast qauadrature, Computer Methods in Applied Mechanics and Engineering 190 (2001) 4339–4364.
[34] T. Nakayama, K. Washizu, The boundary element method applied to the analysis of two-dimensional nonlinear sloshing problems, International Journal for Numerical Methods in Engineering 17 (1981) 1631–1646.
[35] K.J. Bathe, Finite Element Procedures, Prentice-Hall (India), New Delhi, 1996.
[36] F. Brezzi, M. Fortin, Mixed and Hybrid Finite Element Methods, Springer, New York, 1991.
[37] D. Chapelle, K.J. Bathe, The Inf–Sup test, Computers and Structures 47 (1993) 537–545.
[38] K.J. Bathe, The Inf–Sup condition and its evaluation for mixed finite element methods, Computers and Structures 79 (2001) 243–252.
[39] H.N. Abramson, The dynamic behaviour of liquids in moving containers, NASA SP-106, 1966.
[40] T.G.R. Hughes, R.L. Taylor, W. Kanuknukulchal, A simple and efficient finite element for plate bending, International Journal for Numerical Methods in Engineering 11 (1977) 1529–1543.